www.sciencemag.org/cgi/content/full/science.aaa2397/DC1

Supplementary Materials for

Continuous liquid interface production of 3D objects

John R. Tumbleston, David Shirvanyants, Nikita Ermoshkin, Rima Janusziewicz, Ashley R. Johnson, David Kelly, Kai Chen, Robert Pinschmidt, Jason P. Rolland, Alexander Ermoshkin,* Edward T. Samulski,* Joseph M. DeSimone*

*Corresponding author. E-mail: alex@carbon3d.com (A.E.); et@unc.edu (E.T.S.); desimone@email.unc.edu (J.M.D.)

Published 16 March 2015, *Science* **347**, 1349 (2015)
DOI: 10.1126/science.aaa2397

This PDF file includes:

Materials and Methods

Supplementary Text

Figs. S1 to S4

Captions for movies S1 and S2

References

Additional supplementary material for this manuscript includes:

Movies S1 and S2

Materials and Methods

Materials

The ramp test patterns in Fig. 1C were printed with trimethylolpropane triacrylate (TMPTA) using the photoinitiator, diphenyl(2,4,6-trimethyl-benzoyl)phosphine oxide. Other objects were printed with a combination of monomers from Sartomer (CN2920 & CN981), TMPTA, and reactive diluents such as n-vinylpyrrolidone, isobornyl acrylate, and cyclohexane dimethanol di-vinyl ether. We also utilized the photoinitiators, phenylbis(2,4,6-trimethyl-benzoyl)phosphine oxide, 1-hydroxycyclohexyl phenyl ketone, and 2-benzyl-2-(dimethylamino)-4'-morpholinobutyrophenone along with an assortment of dyes from Wikoff and Mayzo.

Methods

The dead zone thickness is measured with a differential thickness technique. As shown in Fig. S3A, a 200 μm aluminum shim is placed between an impermeable glass slide and an oxygen permeable Teflon AF 2400 window. Liquid resin is then sandwiched between these two rigid planes and receives sequences of exposure pulses (1 sec on / 1 sec off for 20 pulses) from the continuous liquid interface printing (CLIP) imaging unit. A thickness indicator is then used to measure the cured thickness on the glass slide, which is subtracted from 200 μm to give the equilibrium dead zone thickness. Multiple dots are cured with the same conditions to increase statistics. The precision of the thickness indicator is 0.5 μm.

Cured thickness is measured in a similar way as shown in Fig. S3B. Resin is placed on a glass slide and illuminated from below with varying dosage from the CLIP imaging unit. Excess resin is then wiped away and the thickness of each dot is measured with a thickness indicator. Both the resin cure dosage (D_c) and absorption coefficient (α) are independent fit parameters and are determined from this measurement. Translation of this measurement, which disregards the dead zone, to CLIP is justified because the dead zone thickness is of order 10X thinner than the cured thickness.

Supplementary Text

Derivation of Eqn. 2

Beginning with the Beer-Lambert absorption law, Φ, the number of photons per unit area per unit time at depth, z, above the build window is given by,

$$\Phi = \Phi_0 e^{-\alpha z} \quad \text{(S1)}$$

where α is the resin absorption coefficient and Φ_0 is the incident photon flux. Taking the derivative of S1 with respect to depth gives the number of absorbed photons per unit area per unit time per unit depth (A),

$$A = \alpha \Phi_0 e^{-\alpha z} \quad \text{(S2)}$$

Multiplying by exposure time (t), gives the total number of absorbed photons per unit area per unit depth (D). This is equivalent to the absorbed photon dosage per unit depth,

$$D = \alpha \Phi_0 t e^{-\alpha z} \quad \text{(S3)}$$

In order for liquid resin to solidify to a particular depth (z_{ct}), a critical absorbed dosage is required for cure. We call this the curing dosage (D_c),

$$D_c = \alpha \Phi_0 t e^{-\alpha z_{ct}} \quad \text{(S4)}$$

Solving for z_{ct} gives the cure thickness as a function of photon dosage ($\Phi_0 t$) and resin parameters, α and D_c,

$$z_{ct} = \frac{1}{\alpha} ln\left(\frac{\alpha \Phi_0 t}{D_c}\right) \quad \text{(S5)}$$

The total absorption coefficient of the resin is given by the sum of the absorption coefficients of the photoinitiator (α_{PI}) and passively absorbing dye (α_{Dye}). Each of these are products of the constituent concentrations and wavelength-dependent absorptivities,

$$\alpha = \alpha_{PI} + \alpha_{Dye} \quad \text{(S6)}$$

In general, D_c increases with addition of passively absorbing dye and can be written in terms of the curing dosage without dye (D_{c0}),

$$D_c = \frac{D_{c0}\,\alpha}{\alpha_{PI}} \quad \text{(S7)}$$

This expression can then be substituted into Eqn. S5 to give Eqn. 2 in the main text,

$$z_{ct} = \frac{1}{\alpha} ln\left(\frac{\alpha_{PI} \Phi_0 t}{D_{c0}}\right) \quad \text{(S8)}$$

Comparison of Eqn. 2 to traditional working curve equation used in stereolithography

Traditionally, the working curve is written in the form (*16*, *19*),

$$z_{ct} = \frac{1}{\alpha} ln\left(\frac{E}{E_c}\right), \quad \text{(S9)}$$

where E and E_c are the actual and critical exposures, respectively, in units of mJ/cm^2. Exposure is synonymous with dosage and is the product of time and flux. We parameterize curing in this work in terms of number of *absorbed* photons (Eqn. 2 and Eqn. S8 above), instead of amount of *incident* energy (Eqn. S9) needed for cure. Describing curing in terms of photon light absorption is more akin to practices used in advanced polymerization modelling (*21*, *29*) and makes switching between different curing wavelengths (that have different photon energy) more straightforward. By setting Eqn. S8 and S9 equal to each other, the more traditional E_c can be written in terms of D_{c0},

$$E_c = 10^{12} \frac{hcD_{c0}}{\lambda \alpha_{PI}}, \quad \text{(S10)}$$

where h is Plank's constant, c is the speed of light, and λ is the peak UV curing wavelength in nm. Finally, making use of Eqn. S7 to rewrite Eqn. S10 in terms of the resin absorption coefficient, α, and curing dosage, D_c, yields

$$E_c = 10^{12} \frac{hcD_c}{\lambda \alpha}. \quad \text{(S11)}$$

We should note that the inhibition from dissolved oxygen in the resin above the dead zone is subsumed in D_{c0}.

Derivation of Eqn. 4

Defining, $\beta \equiv \frac{\alpha_{PI} \Phi_0}{D_{c0}}$, from Eqn. S8 gives:

$$z_{ct} = \frac{1}{\alpha} ln(\beta t) \quad \text{(S12)}$$

Taking the derivative of Eqn. S12 with respect to time gives,

$$\frac{dz_{ct}}{dt} = \frac{1}{\alpha t} \quad \text{(S13)}$$

Using Eqn. S13, the slope of the max speed line that passes through the origin in Fig. S4 is given by,

$$\frac{z_{ct}}{t} = \frac{\frac{1}{\alpha} ln(\beta t)}{t} \quad \text{(S14)}$$

Figure S4 shows z_{ct} as a function of t for different α_{PI} and constant D_{c0}. The maximum speed line intersects each curve at a different z_{ct}. Setting Eqn. S13 equal to Eqn. S14 and solving for exposure time gives the curing time for maximum print speed (t_{max}),

$$t_{max} = \frac{e^1}{\beta} \quad \text{(S15)}$$

Substituting Eqn. S15 into Eqn. S13 or Eqn. S14 gives the maximum print speed (s_{max}),

$$s_{max} = \frac{\beta}{e^1 \alpha} \quad \text{(S16)}$$

Rewriting Eqn. S16 in terms of the absorption height, $h_A = \frac{1}{\alpha}$, gives Eqn. 4 in the main text,

$$s_{max} = \frac{\beta h_A}{e^1} = \frac{\alpha_{PI} \Phi_0 h_A}{e^1 D_{c0}} \quad \text{(S17)}$$

We should note that replenishment of resin in the dead zone by flow upward toward the solidifying part is rapid enough so that α_{PI} does not significantly change during printing. Photobleaching experiments confirmed that very little photoinitiator reacts during the CLIP process, which would reduce α_{PI} (and thus increase h_A) over time.

Notes regarding units

In this work, the following are used:

Φ_0 is the photon flux in units of $\frac{\#}{cm^2 s}$

α is the absorption coefficient in units of $\frac{1}{\mu m}$

D_c is the resin curing dosage in units of $\frac{\#}{cm^2 \mu m}$

s_{max} is the print speed in units of $\frac{\mu m}{s}$. Multiply by 3.6 to convert to mm/hr.

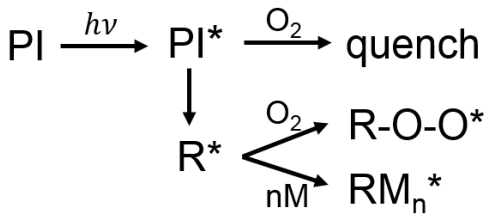

Fig. S1. Free radicals either inhibit oxygen or initiate polymerization.

A photoexcited photoinitiator (PI) can either be quenched with oxygen or cleave to form a radical (R*). The radical can then either react with oxygen to form peroxide or initiate and propagate polymerization (i.e., curing).

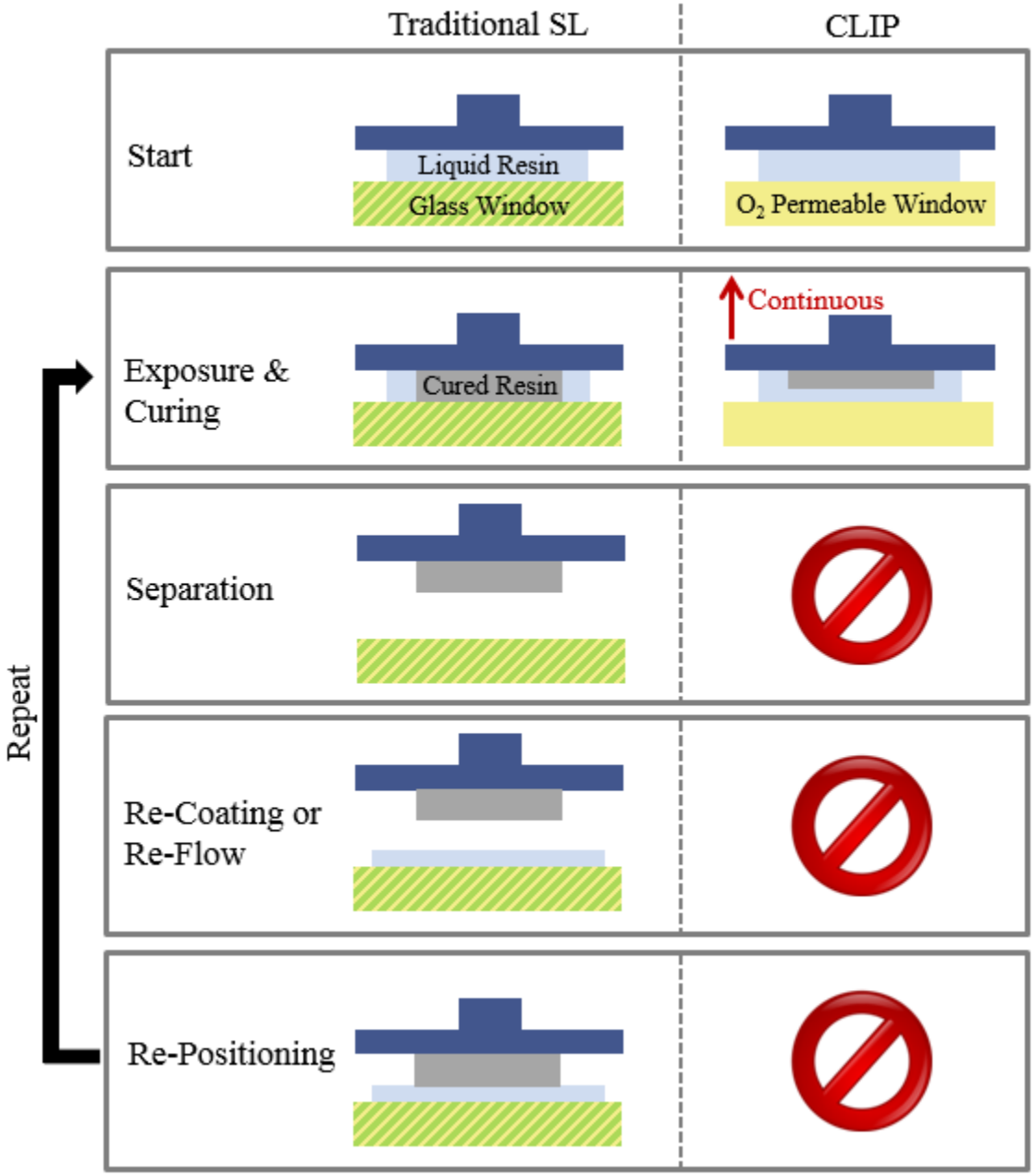

Fig. S2. CLIP removes sequential steps from traditional stereolithography (SL). Traditional stereolithography first exposes resin to UV light, which causes cured adhesion to a build window such as glass. Next, the part must be mechanically separated, followed by resin re-coating and part re-positioning, before the next layer can be exposed. CLIP, with a permanent liquid interface at the window, allows the part to be continuously exposed while elevating, thereby eliminating three steps in the process.

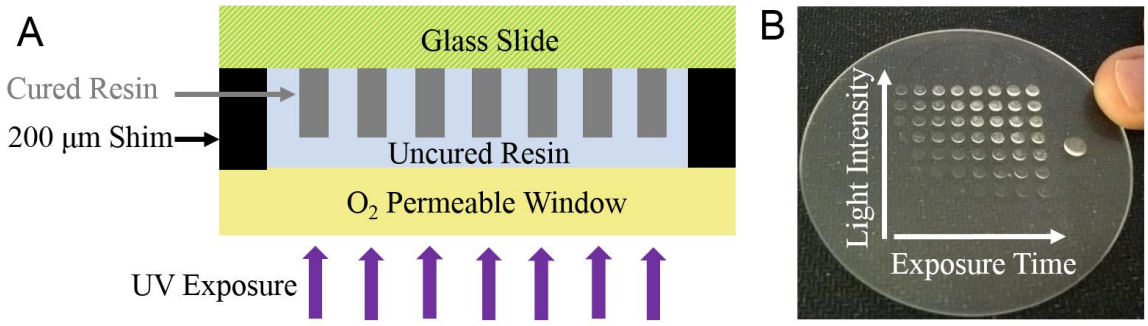

Fig. S3. Measuring dot thickness to quantify dead zone and cure thickness.
(A) Schematic of differential dead zone thickness measurement. (B) Photograph of cured thickness as a function of photon flux and exposure time. Each exposed dot has a diameter of 3 mm.

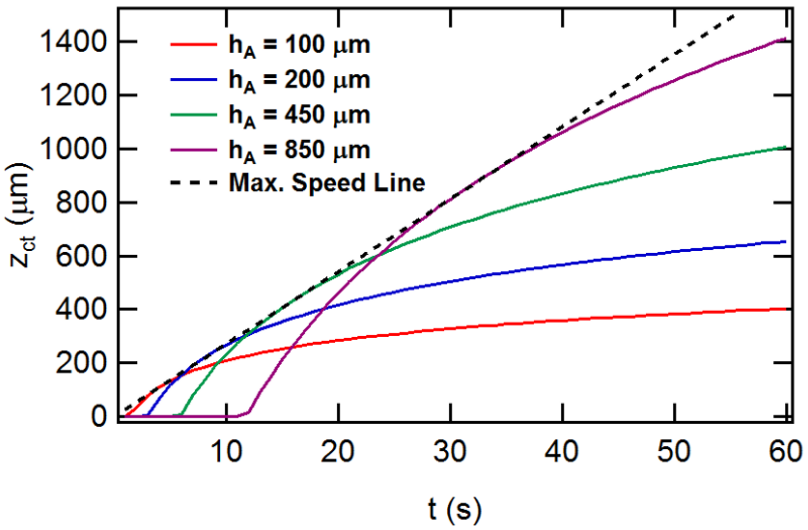

Fig. S4. Maximum print speed is identical for resins with different photoinitiator concentration.

Cured thickness (z_{ct}) as a function of exposure time (t) according to Eqn. S5 for different absorption heights (h_A) (changed by adjusting photoinitiator absorption coefficient (α_{PI}) which also changes resin absorption coefficient (α). No dye is used.). The maximum possible speed print speed occurs at the tangent line with steepest slope that passes through the origin.

Movie S1. Gyroid printed at 500 mm/hr.

The movie play speed is varied from 8X fast-forward to real-time as indicated throughout the movie. Both a measurement ruler and timer are placed beside the printing part for reference. The first two mm of the part is printed below 500 mm/hr to reduce the suction forces when the build support plate is close to the window.

Movie S2. Argyle printed at 500 mm/hr.

The movie play speed is varied from 8X fast-forward to real-time as indicated throughout the movie. Both a measurement ruler and timer are placed beside the printing part for reference. The first two mm of the part is printed below 500 mm/hr to reduce the suction forces when the build support plate is close to the window.

References

1. J. M. Pearce, Building research equipment with free, open-source hardware. *Science* **337**, 1303–1304 (2012). Medline doi:10.1126/science.1228183

2. H. Lipson, M. Kurman, *Fabricated: The New World of 3D Printing* (Wiley, Indianapolis, 2013).

3. B. Derby, Printing and prototyping of tissues and scaffolds. *Science* **338**, 921–926 (2012). Medline doi:10.1126/science.1226340

4. A. Atala, F. K. Kasper, A. G. Mikos, Engineering complex tissues. *Sci. Transl. Med.* **4**, 160rv12 (2012). Medline doi:10.1126/scitranslmed.3004890

5. B. C. Gross, J. L. Erkal, S. Y. Lockwood, C. Chen, D. M. Spence, Evaluation of 3D printing and its potential impact on biotechnology and the chemical sciences. *Anal. Chem.* **86**, 3240–3253 (2014). Medline doi:10.1021/ac403397r

6. K. Sun, T. S. Wei, B. Y. Ahn, J. Y. Seo, S. J. Dillon, J. A. Lewis, 3D printing of interdigitated Li-ion microbattery architectures. *Adv. Mater.* **25**, 4539–4543 (2013). Medline doi:10.1002/adma.201301036

7. G. Chisholm, P. J. Kitson, N. D. Kirkaldy, L. G. Bloor, L. Cronin, 3D printed flow plates for the electrolysis of water: An economic and adaptable approach to device manufacture. *Energy Environ. Sci.* **7**, 3026–3032 (2014). doi:10.1039/C4EE01426J

8. M. D. Symes, P. J. Kitson, J. Yan, C. J. Richmond, G. J. Cooper, R. W. Bowman, T. Vilbrandt, L. Cronin, Integrated 3D-printed reactionware for chemical synthesis and analysis. *Nat. Chem.* **4**, 349–354 (2012). Medline doi:10.1038/nchem.1313

9. P. Chakraborty, R. N. Zuckermann, Coarse-grained, foldable, physical model of the polypeptide chain. *Proc. Natl. Acad. Sci. U.S.A.* **110**, 13368–13373 (2013). Medline doi:10.1073/pnas.1305741110

10. P. J. Kitson, A. Macdonell, S. Tsuda, H. Y. Zang, D.-L. Long, L. Cronin, Bringing crystal structures to reality by three-dimensional printing. *Cryst. Growth Des.* **14**, 2720–2724 (2014). doi:10.1021/cg5003012

11. J. L. Erkal, A. Selimovic, B. C. Gross, S. Y. Lockwood, E. L. Walton, S. McNamara, R. S. Martin, D. M. Spence, 3D printed microfluidic devices with integrated versatile and reusable electrodes. *Lab Chip* **14**, 2023–2032 (2014). Medline doi:10.1039/C4LC00171K

12. X. Zheng, H. Lee, T. H. Weisgraber, M. Shusteff, J. DeOtte, E. B. Duoss, J. D. Kuntz, M. M. Biener, Q. Ge, J. A. Jackson, S. O. Kucheyev, N. X. Fang, C. M. Spadaccini, Ultralight, ultrastiff mechanical metamaterials. *Science* **344**, 1373–1377 (2014). Medline doi:10.1126/science.1252291

13. T. A. Schaedler, A. J. Jacobsen, A. Torrents, A. E. Sorensen, J. Lian, J. R. Greer, L. Valdevit, W. B. Carter, Ultralight metallic microlattices. *Science* **334**, 962–965 (2011). Medline

14. J. Bauer, S. Hengsbach, I. Tesari, R. Schwaiger, O. Kraft, High-strength cellular ceramic composites with 3D microarchitecture. Proc. Natl. Acad. Sci. U.S.A. **111**, 2453–2458 (2014). doi:10.1073/pnas.1315147111

15. E. B. Duoss *et al*., Three-dimensional printing of elastomeric, cellular architectures with negative stiffness. *Adv. Funct. Mater.* **24**, 4905–4913 (2014).

16. I. Gibson, D. W. Rosen, B. Stucker, *Additive Manufacturing Technologies: Rapid Prototyping to Direct Digital Manufacturing* (Springer, New York, 2010).

17. S. C. Ligon, B. Husár, H. Wutzel, R. Holman, R. Liska, Strategies to reduce oxygen inhibition in photoinduced polymerization. *Chem. Rev.* **114**, 557–589 (2014). Medline doi:10.1021/cr3005197

18. Y. Yagci, S. Jockusch, N. J. Turro, Photoinitiated polymerization: Advances, challenges, and opportunities. *Macromolecules* **43**, 6245–6260 (2010). doi:10.1021/ma1007545

19. P. F. Jacobs, *Rapid Prototyping & Manufacturing: Fundamentals of StereoLithography* (Society of Manufacturing Engineers, Dearborn, MI, 1992).

20. T. C. Merkel, I. Pinnau, R. Prabhakar, B. D. Freeman, *Materials Science of Membranes for Gas and Vapor Separation* (Wiley, West Sussex, UK, 2006), pp. 251–270.

21. D. Dendukuri, P. Panda, R. Haghgooie, J. M. Kim, T. A. Hatton, P. S. Doyle, Modeling of oxygen-inhibited free radical photopolymerization in a PDMS microfluidic device. *Macromolecules* **41**, 8547–8556 (2008). doi:10.1021/ma801219w

22. D. Dendukuri, D. C. Pregibon, J. Collins, T. A. Hatton, P. S. Doyle, Continuous-flow lithography for high-throughput microparticle synthesis. *Nat. Mater.* **5**, 365–369 (2006). Medline doi:10.1038/nmat1617

23. J. M. Gonzalez-Meijome, V. Compañ-Moreno, E. Riande, Determination of oxygen permeability in soft contact lenses using a polarographic method: Estimation of relevant physiological parameters. *Ind. Eng. Chem. Res.* **47**, 3619–3629 (2008). doi:10.1021/ie071403b

24. J. A. Rogers, T. Someya, Y. Huang, Materials and mechanics for stretchable electronics. *Science* **327**, 1603–1607 (2010). Medline

25. S. Bauer, S. Bauer-Gogonea, I. Graz, M. Kaltenbrunner, C. Keplinger, R. Schwödiauer, A soft future: From robots and sensor skin to energy harvesters. *Adv. Mater.* **26**, 149–161 (2014). Medline doi:10.1002/adma.201303349

26. N. Travitzky, A. Bonet, B. Dermeik, T. Fey, I. Filbert-Demut, L. Schlier, T. Schlordt, P. Greil, Additive manufacturing of ceramic-based materials. *Adv. Eng. Mater.* **16**, 729–754 (2014). doi:10.1002/adem.201400097

27. C. Cvetkovic, R. Raman, V. Chan, B. J. Williams, M. Tolish, P. Bajaj, M. S. Sakar, H. H. Asada, M. T. Saif, R. Bashir, Three-dimensionally printed biological machines powered by skeletal muscle. *Proc. Natl. Acad. Sci. U.S.A.* **111**, 10125–10130 (2014). Medline doi:10.1073/pnas.1401577111

28. Y. Lu, G. Mapili, G. Suhali, S. Chen, K. Roy, A digital micro-mirror device-based system for the microfabrication of complex, spatially patterned tissue engineering scaffolds. *J. Biomed. Mater. Res. A* **77**, 396–405 (2006). Medline doi:10.1002/jbm.a.30601

29. S. K. Suh, K. W. Bong, T. A. Hatton, P. S. Doyle, Using stop-flow lithography to produce opaque microparticles: Synthesis and modeling. *Langmuir* **27**, 13813–13819 (2011). Medline doi:10.1021/la202796b